Bioprinting xxx (xxxx) xxx

Contents lists available at ScienceDirect

Bioprinting

journal homepage: www.elsevier.com/locate/bprint

Development and characterization of a low-cost 3D bioprinter

Bekir Yenilmez [a], Mikail Temirel [b], Stephanie Knowlton [b], Eric Lepowsky [a], Savas Tasoglu [a,b,c,d,e,*]

[a] Department of Mechanical Engineering, University of Connecticut, Storrs, CT, 06269, United States
[b] Department of Biomedical Engineering, University of Connecticut, Storrs, CT, 06269, United States
[c] Institute of Materials Science, University of Connecticut, Storrs, CT, 06269, United States
[d] Institute for Collaboration on Health, Intervention, and Policy, University of Connecticut, Storrs, CT, 06269, United States
[e] The Connecticut Institute for the Brain and Cognitive Sciences, University of Connecticut, Storrs, CT, 06269, United States

ARTICLE INFO

Keywords:
Bioprinting
Inkjet printing
Extrusion printing
Low-cost bioprinter
Gelatin methacryloyl
Alginate
Open-source bioprinter

ABSTRACT

Bioprinting complex three-dimensional architectures of cell-laden hydrogels is a promising approach for creating custom living tissues. However, it is challenging to fabricate hydrogel-based constructs at both high-throughput and high-resolution; bioprinters that offer both advantages are generally not affordable for most researchers. Thus, there is an unmet need for low-cost, open-source bioprinters. Such an accessible tool will enable rapid design iterations to accelerate the ongoing research and development of biomimetic tissues and biomaterial use. Here, we develop and implement a low-cost hybrid bioprinter using both inkjet and extrusion print heads, which are capable of printing gelatin methacryloyl and alginate, respectively. We characterized the geometric accuracy of the plotter. Moreover, the printing and crosslinking parameters were optimized to maximize the cell viability.

1. Introduction

With an increasing demand for readily available, scaled-up, biomimetic tissues and organs, bioprinting technologies are advancing rapidly. Applications within tissue engineering and regenerative medicine include creating organ-on-a-chip devices for medical and drug discovery research [1,2] and replicating disease tissues such as tumors to better understand the disease process [3,4], regenerating human tissues to replace those which are damaged or diseased [5–7], and conducting stem-cell research [8]. Of particular interest are methods to construct various "bioinks" into complex three-dimensional (3D) designs, including patterning multiple types of bioinks in a single construct, to closely mimic the *in vivo* micro-environment [9–13]. However, while the spatial distribution of cells is critical to direct cell- and tissue-level behavior, it remains a significant challenge to create such complex constructs in a high-throughput manner. As an emerging solution, bioprinting is an attractive technique for high-throughput, repeatable, and precise construction of cell-laden structures on the micro- and macro-scales [14]. However, most commercially available bioprinters are limited by the tradeoff between resolution and throughput; moreover, the bioprinters are expensive and, therefore, inaccessible, ranging from $10,000 to over $200,000.

The foundational concepts behind bioprinting are commensurate with those of the more common 3D printing: material is added to the print in progressive layers to form 3D objects. Bioprinters must be designed to be compatible with cell-laden bioinks, which places limitations on the heating, forces applied in the printing nozzle, and other parameters due to the limited range of biocompatible materials available as well as the need to maintain cell viability throughout the process. A range of bioprinters have been proposed which achieve this with various bioinks, including most ubiquitously extrusion-based printing using filaments, inkjet printing of liquid droplets, and laser-assisted bioprinting [15]. While inkjet-based bioprinting generally offers superior resolution, it is a challenge to implement it with certain biomaterials because it is only compatible with low-viscosity bioinks.

Hydrogels have been shown to serve as an excellent extracellular matrix (ECM) to facilitate cell growth [16,17]. One ECM scaffold which shows great promise is gelatin methacryloyl (GelMA) [18]. GelMA is an inexpensive and cell-responsive biomaterial naturally derived from denatured collagen, a very common structural protein in the body, and chemically modified with a methacrylate group. Cells have been shown in many studies to survive, grow, and even form functional 3D networks within scaffolds of various materials, particularly those made of naturally derived materials like GelMA and alginate.

* Corresponding author. Department of Mechanical Engineering, University of Connecticut, Storrs, CT, 06269, United States.
E-mail address: savas.tasoglu@uconn.edu (S. Tasoglu).

https://doi.org/10.1016/j.bprint.2019.e00044
Received 24 July 2018; Received in revised form 17 December 2018; Accepted 29 January 2019

Please cite this article as: B. Yenilmez et al., Development and characterization of a low-cost 3D bioprinter, Bioprinting, https://doi.org/10.1016/j.bprint.2019.e00044

Bertassoni et al. implemented a block-based bioprinting technique to print with GelMA by crosslinking and extruding 30 mm by up to 65 mm building blocks one at a time [19]; however, this approach is limited by the block size. An extrusion-based approach developed by Kolesky et al. used a fugitive ink, pluronic F127, as a support material into which the GelMA matrix was printed and photocrosslinked and subsequently removed by cooling to 4 °C [20]. Zhu et al. used a stereolithography-based bioprinter to encapsulate neural stem cells in a GelMA-based bioink with graphene nanoplatelets [21]. Inkjet-based bioprinters have been implemented with a limited range of bioinks; Gao et al. used a blend of polyethylene glycol and GelMA to tune the bioink properties to be compatible with an inkjet printer. However, to our knowledge, inkjet bioprinting has not been applied successfully to pure GelMA, which is desirable to take full advantage of the cell-supportive properties of the material.

Alginate is another biomaterial that has been studied extensively [22], particularly for bone [23] and cartilage [23] tissue engineering. While mammalian cells do not attach to unmodified alginates, the structure can be readily modified with domains such as RGD to facilitate cell attachment and growth [22]. It is readily crosslinked by mixing with calcium (such as calcium chloride). A few bioprinters compatible with alginate have been proposed. Park et al. studied different compositions of alginate bioinks, finding that high- and low-molecular-weight alginate can be mixed to facilitate cell growth [24]. Alginate is often blended with other materials to improve its printability and cytocompatibility. For example, Schutz et al. added 3% methylcellulose to improve the viscosity and thereby facilitate deposition [25].

Here, we propose a custom bioprinter leveraging both inkjet and extrusion printing (Fig. 1) and demonstrate their abilities to print cell-laden GelMA and alginate, respectively. It is capable of printing of custom designs and structures by using a CNC XYZ stage as a platform. Bioink is deposited from a reservoir of biomaterial through one of the two print heads and onto the printing bed.

The inkjet head relies on photocrosslinkability and temperature-dependent viscosity transition of GelMA. Upon exposure to light in the presence of a photoinitiator, these methacrylate groups crosslink with one another, forming a structural network on which cells can grow. This feature offers temporal control over the material properties of the bioink simply by applying UV light. Thus, GelMA can be compatible with inkjet printing as a low-viscosity bioink before crosslinking, then be imparted with the mechanical properties needed to maintain the printed structure after crosslinking. Photocrosslinking is mediated by a photoinitiator, such as Irgacure 2959, which initiates crosslinking in the far UV light range (280 nm, although longer UV wavelengths up to 365 are often used with slightly lower efficiency), or lithium phenyl-2,4,6-trimethylbenzoylphosphinate (LAP), which initiates crosslinking in the blue light range (405 nm) [26]. It should also be noted that LAP has been shown to have a lower cytotoxicity than some other photoinitiators. We also take advantage of the documented temperature-dependent change in viscosity [20]: the shear elastic modulus of uncrosslinked GelMA changes from above 10^4 Pa at 4 °C to approximately 10^{-2} Pa at 37 °C. Similar to the application of light, the application of heat is controlled such that the bioink is heated in the printer head to attain a low viscosity, then as it cools on the printing platform, it attains a higher viscosity.

In addition to the inkjet head, the extrusion-based printing head is comprised of a coaxial printing head, which is a widely reported extrusion method [12,27–30]. Alginate is co-extruded with a stream of calcium chloride in the center to crosslink the structure. While this extrusion-based printing is lower in resolution, as the resolution is mainly limited by the width of the extruded filament, it provides a relatively high-throughput compared to inkjet printing. Thus, the hybrid bioprinter is expected to leverage the unique benefits of both extrusion

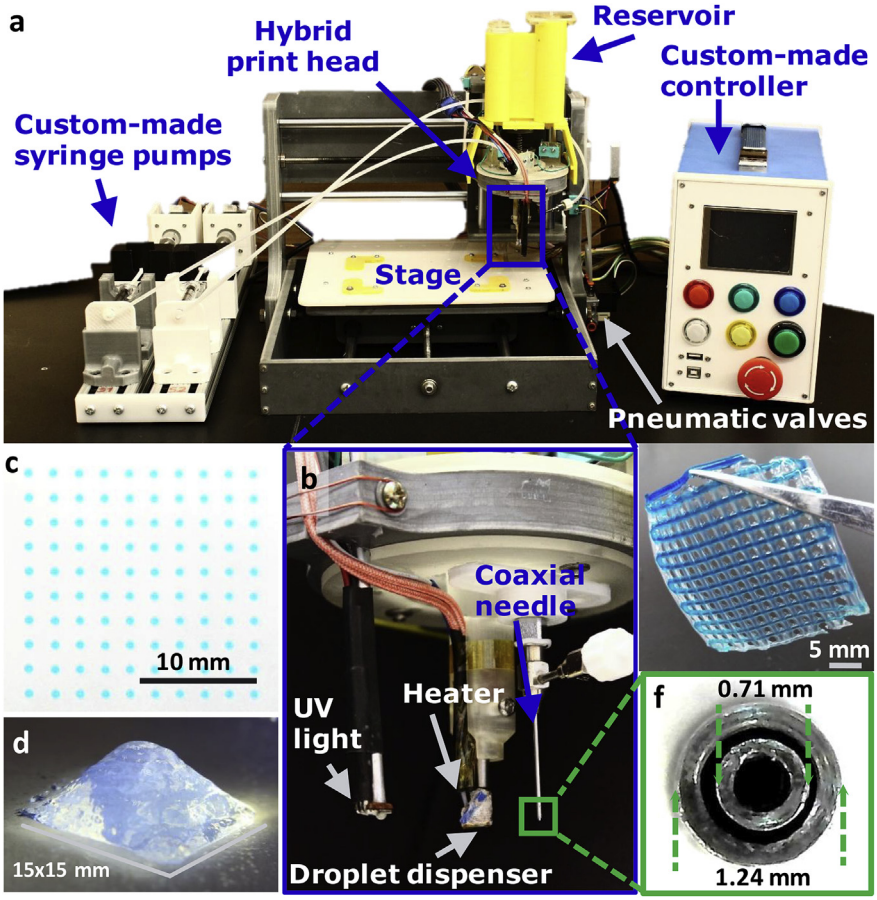

Fig. 1. (**a**) Overview of the proposed hybrid bioprinter (see Fig. S1 for the details of control box) and (**b**) a close-up of the printing heads including a droplet dispenser for inkjet printing, a UV light for crosslinking the bioink following deposition, and a coaxial needed for extrusion printing. (**c–d**) Demonstration of the inkjet printing showing (**c**) individual droplets and (**d**) a 3D 21-layer pyramid. (**e–f**) Demonstration of extrusion printing showing (**e**) an image of a printed mat where the second layer is printed perpendicular to the first and dyed blue for better visulalization and (**f**) a close-up of the printing head with two inputs for alginate and $CaCl_2$.

and inkjet printing.

Herein, we characterize the spatial precision of the individual drops from the inkjet print head, which are used to create the desired density and infill of the printed structure. We then measured the distribution of light to cure the deposited GelMA while also preserving the viability of cells suspended in the hydrogel. In addition, we characterize the filament and channel diameter of the extruded prints with respect to the print head speed for the extrusion print head. The viability of cells printed from both print heads was characterized to optimize the printing parameters. The results demonstrate the feasibility of the proposed hybrid droplet-and-extrusion-based bioprinter.

2. Methods

2.1. Mechanical design

The bioprinter (Fig. 1a) is based on a gantry-type three-axis CNC stage (2020B, Konmison, China) where the X and Z axis are on the gantry and the Y axis is on the worktable. A custom head was designed (Fig. 1b) to hold the 405 nm near-UV led (Luminus Devices Inc., MA, US), a sub-microliter dispensing valve G150-G1501000 (TechElan llc, NJ, US), a coaxial syringe tip (Rame-hart Instrument Co.,NJ, US), and a custom syringe holder. For the droplet printing, a 90 psi pressurized air source was regulated to the desired pressure (15–45 psi) using a miniature air pressure regulator PPR2-N02BG-4 (PneumaticPlus, CA, US) and connected to the syringe through a solenoid valve VQ110U-5M (SMC, Tokyo, JP). For the extrusion printing, two custom syringe pumps were designed (see supplementary information) and connected to the coaxial needle tip. When the printer is in operation, three motors (namely x- y- and z-directions) were used to control the motion of the syringe on three directions. To protect the dispenser head from unexpected impacts, microswitches (uxcell, Hong Kong, China) detect if the nozzle hits an obstruction and automatically stops movement. The sample (such as GelMA) loaded in the syringe was ejected from the nozzle followed by curing by the UV light (Fig. 1b) for droplet-based printing, whereas alginate cured chemically for extrusion-based printing.

2.2. Electrical design

The movement of the axis is controlled with an Osoyoo MKS Gen 1.5 3D printer controller (Pinetree Electronis Ltd, Canada) loaded with the open-sourced Marlin firmware. The solenoid valve is controlled with the same board through a MOSFET driver board (FlamingoEDA, Beijing, China).

2.3. Production and modification of G-Code

The designs for 2D printed objects were created with a custom MATLAB (Mathworks, MA, US) GUI, where the user can select from available patterns, modify their parameters and export it as G-code. The designs for 3D printed objects were created in SolidWorks 2017 (Dassault Systèmes SolidWorks Corp., Waltham, MA), a professional computer aided design software, and saved as an STL file. Slic3r (version 1.2.9 stable), a free open sourced 3D printing processing software, was used as the slicing engine to produce the G-code file for 3D STLs. The G-code files, either from the GUI or from Slic3r, were then loaded into Repetier-Host (version 1.6.2), a free 3D printing software interface (Hot-World GmbH & Co. KG, Willich, Germany) which controls the bioprinter connected to the computer through a USB port. This process is further described in the supplementary file and depicted in Fig. S2.

2.4. Bioink preparation

GelMA was synthesized as outlined in Ref. [18] and prepared at a final concentration of 50 mg/mL in PBS (phosphate buffered saline) with 0.5% LAP (Biobots, Philadelphia, PA, US) at 37 °C. The bioink was filtered through a 0.2 μm sterile filter before use to remove and particles that may clog the printhead. National Institutes of Health (NIH) 3T3 mouse embryonic fibroblast cells (ATCC, US) were then trypsinized to prepare a single-cell suspension and added to the bioink at a concentration of approximately 3 million cells/mL immediately before printing. The bioink was protected from light during preparation to avoid unintended crosslinking.

Sodium alginate powder (Sigma-Aldrich, US) was added to PBS at a concentration of 2% 4%, 6%, or 8% (w/v) and vortexed for 1 min at 3400 rpm. The solution was then kept in the oven at 37 °C overnight to dissolve the alginate. The bioink solution was filtered through a 5 μm sterile filter and mixed with cells as described for GelMA. The bioink was then loaded into 10 mL syringes. The ionic cross-linker, calcium chloride ($CaCI_2$) (Sigma-Aldrich, US), was dissolved in PBS at 2% (w/v) by mixing on a vortex at 3400 rpm for 1 min and loaded into another into 10 mL syringe.

2.5. Printing parameters

For inkjet-printing, the prepared bioink was loaded into the sterilized reservoir. A pressure of 10 psi was applied to the bioink reservoir and 24 V was applied to the solenoid for 56.25 μs to form each drop as the print head moved along the x- and y-axes. Each layer was crosslinked immediately after printing and once the entire print was deposited and crosslinked, PBS was applied immediately. For prints with encapsulated cells, the prints were subsequently washed twice with cell media at 10-min intervals and then incubated in complete cell media at 37 °C with 5% CO_2.

For the spatial accuracy characterization, GelMA with fabric dye was used as the bioink to create a 20 × 20 mm grid pattern. The printed pattern is imaged with a camera and image processing is done through MATLAB to detect the center points of each dot and calculate the deflection of the dots as compared to their expected location.

The exposure pattern of the UV curing light was characterized by exposing SunArt Paper (TEDCO Toys, USA) for various times: 1, 10, 20, and 30 s. The SunArt Paper is developed by UV light according to the amount of exposure received, similar to the process by photography film is exposed. The curing light was positioned 5 mm above the paper during exposure to mimic the height between the light and well plates used during printing. These exposed papers were then digitalized using a flatbed scanner and analyzed in MATLAB to determine the normalized intensity and exposure pattern.

For extrusion-printing, the prepared syringes with the bioink and 2% $CaCI_2$ were placed on the two different syringe pumps and the flow rates were set to 0.15 and 0.1 mL/m, respectively. The nozzle speed was set to 6 mm/s. The bioink was deposited on glass slides in a grid pattern. After printing, the samples were transferred into a well plate. Warm PBS was applied immediately followed by two washes with cell media and the samples were finally incubated in cell media.

2.6. Viability characterization

To characterize the cell viability and proliferation of inkjet-printed cells, immunocytochemistry of proliferating cells was accomplished by staining with DAPI (blue), Ki67 (red), and Phalloidin (green). The cell-encapsulating hydrogels were fixed with 1% paraformaldehyde for 1 h at room temperature and subsequently washed. The cells were permeabilized with 0.3% Triton-X 100 (Sigma), in 1% BSA (Sigma), for a minimum of 1 h at room temperature. First, the hydrogels were stained with Rb mKi67 (Ab16667, Abcam) overnight at 4 °C. After washing, the hydrogels were incubated with secondary antibody goat anti rabbit Alexa Fluor 564 (A11011, Invitrogen) for 2 h at room temperature. Actin cytoskeletons were visualized with phalloidin, while DAPI was used for nuclear counter staining. After washing, the hydrogels were observed and imaged under a fluorescent microscope (Zeiss AXIO).

For cell viability, calcein AM (which stains live cells green) and

ethidium homodimer-1 (EthD, which stains dead cells red) stains were used (Life Technologies). The stained cells were then observed under a fluorescence microscope. The constructs were washed once with PBS and then a solution of 1:2000 calcein and 1:500 ethidium homodimer in PBS was applied. Each sample was thoroughly covered with the staining solution and then incubated for 15 min. After the 15 min incubation period at room temperature, the staining solution was aspirated and all the samples were washed with PBS for imaging. Images were captured from six different focal planes over a z-axis range of 250 μm in different areas of each print. To quantify the cell viability using calcein and EthD, the six images were combined into a z-stack and the maximum value of each (x,y) pixel across all six planes was used to create a z-projection image for each channel separately. From each image, the "find maxima" function in ImageJ [31] was used with a noise tolerance value of 20 to identify local maxima in the image; each local maximum in the green-channel (calcein) image was taken as a live cell and each local maximum in the red-channel (EthD) image was taken as a dead cell. Then, the viability in each image was calculated as $\frac{live\ cells}{dead\ cells+live\ cells}$. The average viability for each crosslinking time was taken as the total number of live cells divided by the total number of cells (live and dead) counted across several images from two different prints. The composite images shown are pseudo-colored to show both calcein and EthD staining in a single image.

3. Results

3.1. Spatial accuracy with inkjet printing

Spatial resolution in this system depends on both the droplet size and where the droplets are deposited by the printer head. Droplets are formed by the solenoid-driven dispensing valve. The dispensing valve is positioned within a solenoid, which acts as an electromagnet to control the dispensing valve. When a voltage is passed through the solenoid, the induced magnetic field causes the dispensing valve to open. By controlling the duration of time that the dispensing valve remains open and the pressure at which the bioink is supplied to the dispensing valve, the droplet formation was manipulated. Once deposited, each droplet (created at 10 psi and 56.25 μs timing value) spreads to a diameter of approximately 531.71 ± 48.87 μm as shown in Fig. 2a. The deflection of each dot relative to its expected position is characterized by printing a grid pattern and comparing the X- and Y-deflections of these droplets relative to the intended positions (Fig. 2b). It is seen that the standard deviation is 0.0568 mm and 0.0624 mm for X- and Y-axis, respectively. To check the accuracy of this test method, the same procedure is repeated with an office laser printer. The deflection of a reference pattern printed using a laser printer returned a standard deviation of 0.0440 mm and 0.0437 mm for X- and Y-axis. With the resolution of 45 pixels per millimeter for the imaging setup, the standard deviation of the bioprinter was within the range of 1–2 pixels.

3.2. Light distribution in the build area

The light exposure across the build area influences how the print will be crosslinked and therefore defines the build area. The intensity of the UV light output was tested by using an OmniCure radiometer (Model No. R2000, Lumen Dynamics Group Inc). The measured power output was 317 mW/cm^2. The results of the SunArt Paper showed a bullseye-like (concentric circles) exposure pattern for all exposure times tested, as seen in Fig. 2c. For the 1 s exposure, the area of full intensity was limited to a circle of approximately 10 mm diameter, while a diameter of 25 mm received at least 50% UV exposure. As the exposure time increased, the area of exposure can be seen to increase up to 20 s, at which point the exposed area seems to plateau. For the 30 s exposure time, the area of full intensity was approximately 23 mm in diameter, and the 50% exposure region was approximately 35 mm in diameter.

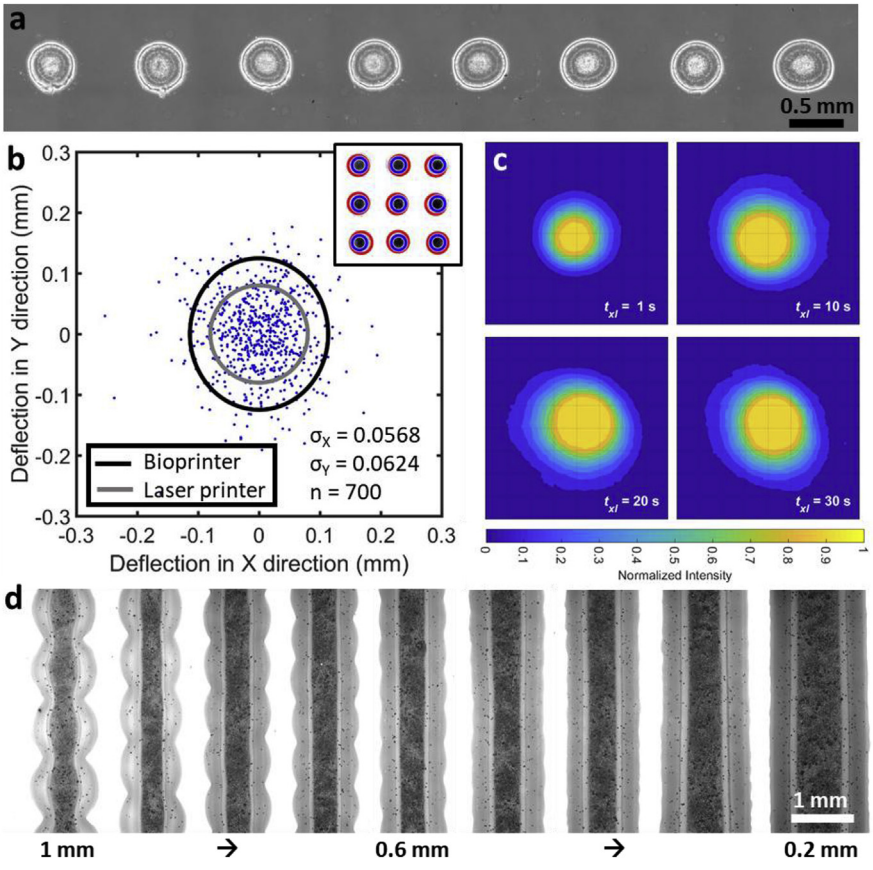

Fig. 2. (**a**) Close-up image of droplets formed by the solenoid valve at the chosen printing parameters. (**b**) The deflection in the x- and y-direction between the intended and actual droplet positions detected using image processing as shown in the inset at the top right; the 2-standard deviation ellipse is shown relative to the accuracy of a laser-printed pattern. (**c**) Light distribution patterns of the curing light for various exposure times: 1 s, 10 s, 20 s, an 30 s expsoure times. All exposures show a bullseye light distribution pattern. Full intensity UV exposure occurred within a 10 mm diameter at 1 s exposure, while for exposures of 20 s and greater experienced a 20 + mm diamter region of full exposure. (**d**) Inkjet-printed lines with varying droplet spacings.

3.3. Droplet spacing for inkjet printing

Because the bioink is deposited as droplets in inkjet printing rather than as a continuous filament, it was necessary to optimize the spacing between the droplets to obtain a continuous line. Several different droplet spacings were tested in the range of 0.2–1 mm as shown in Fig. 2d. When the droplet spacing was decreased to 0.6 mm, the droplets began to merge into a line; however, further decreasing the droplet spacing resulted in the deposition of additional bioink per unit length of the printed line, resulting in spreading of the material over the surface and thickening of the line, which would negatively impact the spatial resolution of this printing process. Therefore, a droplet spacing of 0.6 mm was selected and used herein.

3.4. Nozzle speed for extrusion printing

In order to choose the optimum nozzle speed for the extrusion printing, the print head speed was characterized in terms of channel and filament diameters. The flow rate was held constant at 0.15 mL/min for alginate and 0.1 mL/min for calcium. Two alginate concentrations of 4 and 6% w/v were tested with constant $CaCI_2$ concentration of 2% w/v. A 5 cm line was printed on a glass slide with varying print head speeds from 1 mm/s to 7 mm/m. Blue dye was injected to the channel via a 30G syringe needle to make the channel visible. Then, images were taken using a Canon DSLR camera for all speeds. Fig. 3a shows the effect of nozzle speed on the channel and filament sizes. At low speeds, the channel is noticeably wavy with accumulation of extra material. When the speed increases, the shape of channel obtains the desired straight form and its diameter decreases slightly. Fig. 3b shows the quantitative result of speed test for two alginate concentrations. The channel diameter does not significantly change for either concentration, while the filament diameter decreases with increasing nozzle speed. For low speeds, the hollow channel has a large wall thickness because the $CaCI_2$ crosslinks the alginate immediately when it exits the needle. The $CaCI_2$ then diffuses outwards from the center, resulting in a larger wall thickness for lower speeds since there is more time for the diffusion to occur. Moreover, there was a slight difference in the filament diameter between 4% and 6% alginate concentrations for low speeds. This may be caused by the higher viscosity of 6% alginate preventing the diffusion of $CaCI_2$. In conclusion, the 6 mm/s nozzle speed was chosen as an optimum speed in terms of the channel diameter, filament diameter, and wall thickness.

3.5. Alginate and $CaCl_2$ flow rates for extrusion

Fig. 3c shows the effect of alginate concentration on the channel and filament diameters for varying $CaCI_2$ flow rates at constant nozzle speed of 6 mm/s and constant 2% w/v $CaCI_2$ concentration. As seen in the speed test, channel diameter did not significantly change with varying alginate concentrations from 2 to 8% w/v. Furthermore, alginate and $CaCI_2$ flow rates did not affect the channel diameter significantly, evidenced by the overlapping error bars for all alginate $CaCI_2$ flow rates. However, filament diameter changed slightly with alginate

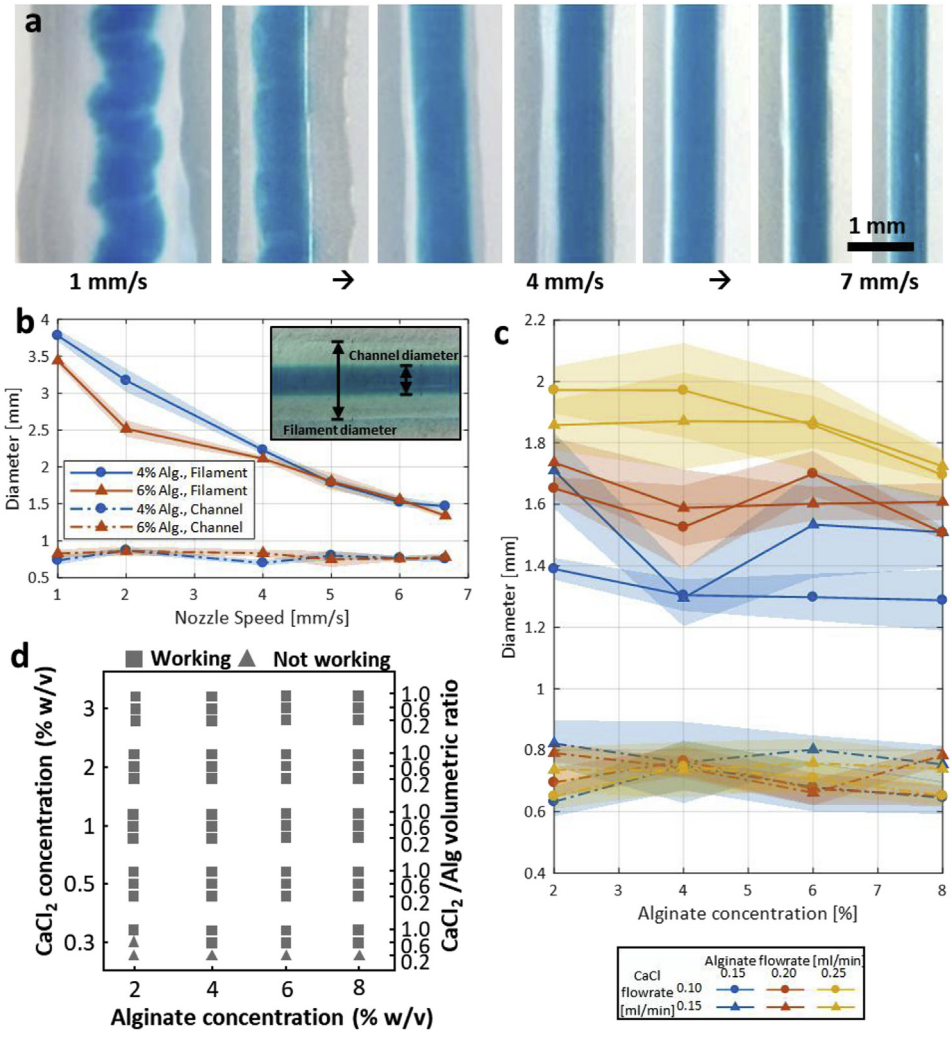

Fig. 3. Characterization of alginate bioink and coaxial extrusion print head. (a) Lines printed by extrusion at various print head speeds, showing the effect of the head speed on the filament and channal diameter. (**b**) Quantative results of speed test that shows the effect of nozzle speed on the filament and channel diameter for two different alginate concentrations. (**c**) Alginate concentrations versus filament and channel diameter with different feading rates. (**d**) Printability with several possible combinations of $CaCl_2$ and alginate concentrations that can be used to obtain effective prints.

concentrations and flow rates. 2% alginate has larger filament diameter in all flow rates because of its low viscosity. It spreads out more when the alginate is deposited from the nozzles as compared to the higher viscosities. The diameter slightly decreased for 8% alginate due to the high viscosity which prevents spreading. Moreover, filament diameter increases with increasing of the alginate flow rate due to the deposition of more bioink. The filament diameter was not significantly affected by the $CaCl_2$ concentration. For all plotted values, each data points represents the measurements of 3 repetitions.

Fig. 3d shows a performance chart for the extrusion process (i.e. depositing $CaCl_2$ through the 22G inner nozzle while depositing alginate via the 18G outer nozzle). The successful formation of the hollow channel was observed with certain combinations of alginate and $CaCl_2$ concentrations and certain volumetric ratios of these components as indicated by the squares in the figure. Moreover, it was found that the 8% w/v alginate concentration is the maximum concentration compatible with the needle sizes used; higher concentrations are not compatible due their high viscosity. However, the use of lower alginate concentrations is preferred as the 8% alginate solution could not be sterilized by filtration due to its high viscosity, thereby presenting a high risk of contamination.

3.6. Cell viability

For the inkjet-printed cells, the crosslinking time was varied to determine its effect on cell viability. As a control, the cell viability within precursor GelMA solution without being printed was used. The hydrogel was not sufficiently crosslinked and dissolved during the incubation period with crosslinking times lower than 20 s. However, with crosslinking times between 20 and 30 s, the cell viability did not vary significantly. For longer crosslinking times, cell viability decreased. With 25 s or more crosslinking time, there is a notable decline in cell viability along the edge of the construct and the width of this reduced viability region on the edge expands as the crosslinking time decreases, which gives rise to the decreasing trend in viability measured in these gels. This may be attributed to the stresses exerted on the cells as the hydrogel meets the build platform and spreads, due to drying of the gel between when the droplets are deposited and PBS is added, or because excess UV light is focused on the cells in this region as the layer of bioink is thinner. With the crosslinking time optimized, the cell viability and proliferation were studied. Fig. 4a–c shows fluorescence images of inkjet-printed NIH 3T3 mouse embryonic fibroblast cells in GelMA seven days after bioprinting. The viability was quantified over the course of the week, where the viability on day 0, 1, 2, 3, and 7 was 92%, 90%, 87%, 91%, and 93%, respectively, as summarized in Fig. 4d.

For extrusion-printed alginate constructs, the alginate concentration was varied to characterize the effect of the alginate concentration on the cell viability with a constant calcium concentration of 2% (w/v). The cell viability results for varying alginate concentrations are summarized in Fig. 4f. The highest viability of 88% was observed in 4% alginate on day 3, decreasing slightly to 80% on day 7, possibly due to competition for oxygen and nutrients. The fluorescence image of extrusion-printed cells showing the cell viability after three days in 4% alginate is shown in Fig. 4e. For 6% alginate, the viability was 64% at day 3 and decreased to 47% viability at day 7. The decreases might be caused by contamination. The viability was around 50% on days 3 and 7 in the 2% and 8% alginate prints. The low viability observed with the low alginate concentration can be attributed to the weak crosslinking and corresponding degradation of the construct, as well as the low structural integrity of the 2% alginate prints. The low viability observed with higher alginate concentrations can be attributed to the high viscosity, which results in high pressures inside the reservoir during printing, which can stress the cell membrane and result in cell death. Thus, the optimum alginate concentration was concluded to be 4% in terms of both the resulting viability and the printability due to the viscosity.

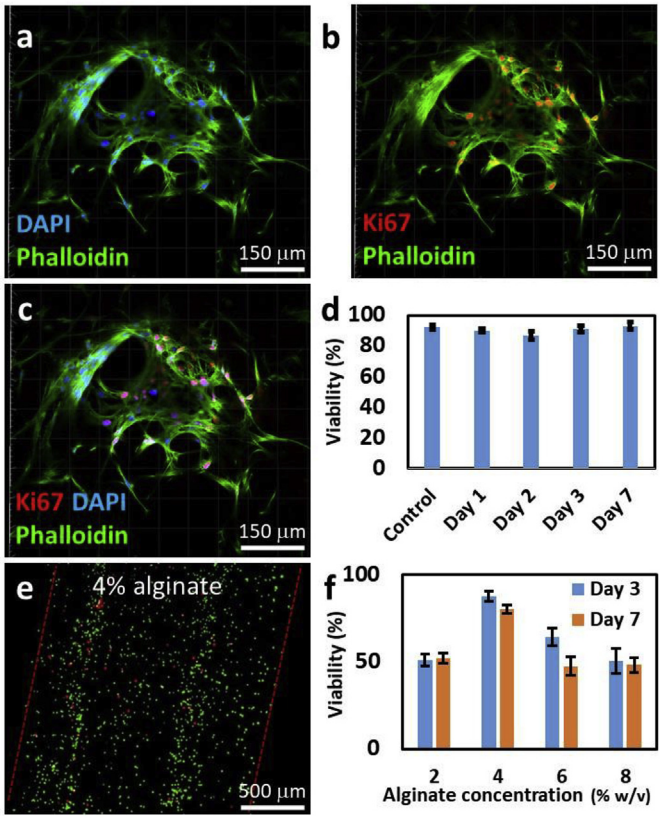

Fig. 4. Characterization of cell viability in inkjet-printed GelMA and extrusion-printed alginate constructs. (a–c) Fluorescence images of inkjet-printed National Institutes of Health (NIH) 3T3 mouse embryonic fibroblast cells in GelMA showing the cell viability after seven days. The constructs are stained with DAPI (blue), Ki67 (red), and Phalloidin (green). (**d**) Viability of inkjet-printed cells over seven days: 92%, 90%, 87%, 91%, and 93% for control (day 0), day 1, 2, 3, and 7, respectively. (**e**) Fluorescence image of extrusion-printed cells showing the cell viability after three days in 4% alginate. The image shown is the Z-axis projection of six two-channel fluorescence images taken over the entire height of the constructs. (**f**) Quantification of the cell viability after seven days with a range of alginate concentrations demonstrating that 4% alginate results in the highest cell viability. (For interpretation of the references to color in this figure legend, the reader is referred to the Web version of this article.)

3.7. Characterization of 3D fabrication

3D patterns were fabricated by successive layers of printing followed by curing. To demonstrate the 3D printing capabilities of the proposed bioprinter, the University of Connecticut (UConn) wordmark was 3D printed using the inkjet head, as shown in Fig. 5a. Each layer was first printed then cured for 20 s under the near-UV light, and then the next layer is printed on top; this was repeated several times to form the finalized print. The multi-layer 15 mm square-based pyramid print in Fig. 1d was printed with 21 layers. Fig. 5b shows how the layers are constructed using the extrusion print head. The first layer is undyed while a blue food color was added to the second layer for contrast. It shows that fluid can pass through the hollow channel.

To quantify the approximate layer heights of the 3D prints, successive layers of a solid/filled 1 cm square were printed and imaged. Images were captured during the process (Fig. S3a shows the inkjet prints and Fig. S3b shows the extruded prints). The images shown in Fig. S3a were processed to determine the total height of each print (in microns). The height of each print was measured both immediately after printing and after swelling in PBS. The inkjet and extruded print heights plotted in Fig. 5c and d, respectively, show that there is a near-linear trend in the as-

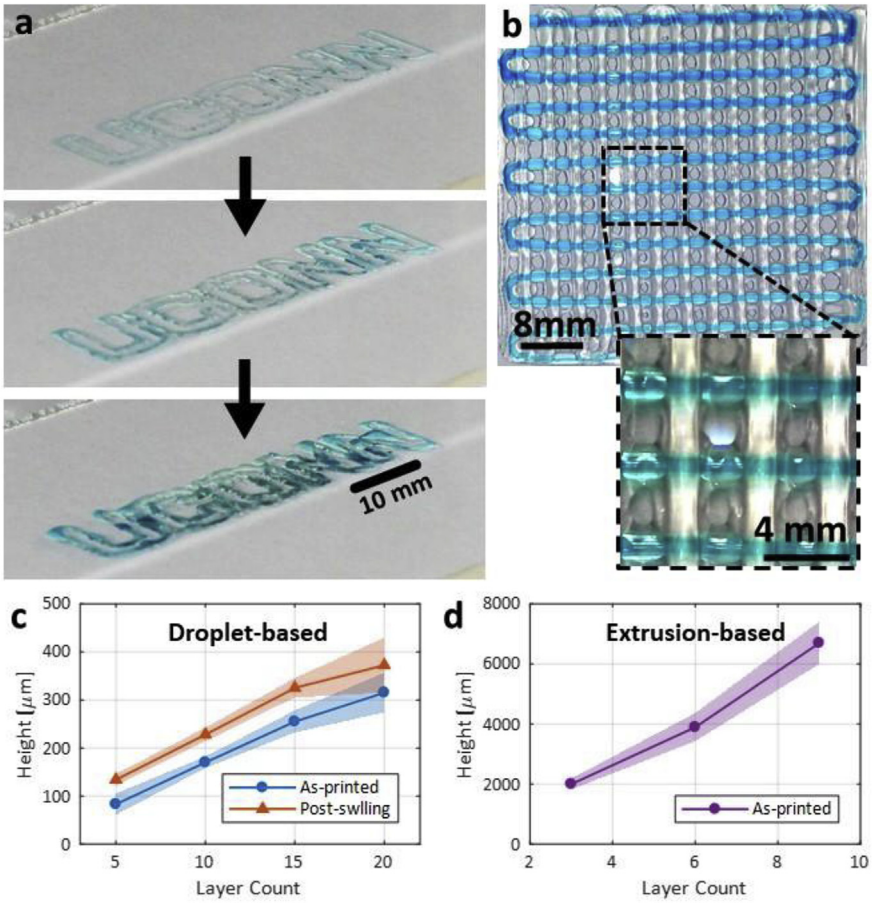

Fig. 5. (**a**) Multi-layer inkjet print of the "UConn" logo, demonstrating a complex-design 3D print. (**b**) Two-layer extrusion print where the second layer is printed perpendicular to the first and dyed blue for better visulalization. **c**) Layers vs. total height in the multi-layer prints shown in (**a**) immediately after printing and after swelling in PBS. (**d**) Layers vs. total height in the extruded multi-layer prints.

printed height although there was slightly more variation in the post-swelling heights. Accordingly, it can be concluded that each inkjet-printed layer has a relatively constant printed height of 16.5 ± 2.3 μm while each extruded layer has a printed height of 700 ± 83 μm. This further highlights the higher resolution that is possible with the inkjet print head while also demonstrating the higher throughput that can be achieved with the extrusion head.

3.8. Cost analysis

In addition to the unique capabilities of the proposed design, it is relatively inexpensive compared to commercial bioprinters, totaling approximately $1370. As a point of comparison, two bioprinter companies to consider are labelled here as company A and B, due to the imposed confidentiality on the given quotes. Company A offers four 3D bioprinters with one, two, three, and six pneumatic extruders, with increasing precision as the number of extruders increases, each costing $8,750, $15,250, $26,500, and $50,250, respectively. Even the most affordable of these extrusion-only printers costs over 6-fold the cost of our developed bioprinter. A 3D Bioprinter by company B, which has two separate pneumatic-based extruders, costs $11,840. A more robust, triple-extruder 3D Bioprinter by the same company, which features swappable print heads, totals to $29,140 after factoring in the cost of the swappable print heads for printing thermo-plastics, syringe-based printing, cooled pneumatic printing, and inkjet printing, and additional head for an HD camera. These commercially-available bioprinters are also 8- and 21-fold the cost of our developed bioprinter.

Approximately 36% of the total cost of the proposed bioprinter was from the mechanical components and another 36% was for the two different print heads. The custom syringe pumps account for 11% of the cost. The remaining 17% was for the electrical components of the device (Table 1). A more detailed cost breakdown is provided in Table S1 in the supplementary file. It should be noted that to simplify the build process of our bioprinter, we purchased readily available components, which included a single CNC unit with its carving head included, despite the fact that we removed the head and replaced it with our custom bioprinter heads. In nearly any case, buying a complete single unit will be costlier than a bulk purchase of just the needed component(s). For instance, a bulk purchase of multiple CNC frames without the associated head can reduce the cost of our bioprinter.

4. Conclusion

By leveraging the capabilities of various modes of 3D printing and the biocompatibility of different hydrogels, we have developed a low-cost hybrid droplet-and-extrusion-based bioprinter to address the increasing demand for readily available biomimetic tissues and organs. This

Table 1
Cost breakdown of the custom-developed printer.

Component	Total Price
Mechanical parts	$ 493
Electronics	$ 232
Printing heads	$ 495
Syringe pumps	$ 150
Total	**$ 1370**

bioprinter is capable of direct-write bioprinting of hydrogel material in multiple layers balancing both high-resolution (using the inkjet head and photo-crosslinking) and high-throughput (using the extrusion head and chemical-crosslinking). We characterized the effectiveness of both modes of printing in various 2D and 3D custom designs and structures. To validate this approach for tissue engineering, we characterized the cell viability of mouse fibroblast cells over time. Future work will aim to integrate the two printing modes together and to characterize the viability of larger prints by using the hollow channels in the alginate to distribute oxygen and nutrients into the bulk of the printed tissues, where diffusion is insufficient, and evaluate the homogeneity of cell-laden prints comprising multiple hydrogels. Furthermore, our platform can be benchmarked for other hydrogels and polymers, in addition to the GelMA and alginate reported, by adjusting the printer settings and parameters, such as the rate of extrusion and the droplet dispensing timing and pressure.

Acknowledgements

ST acknowledges the Connecticut Innovations Biopipeline Award “A Versatile and Low-Cost Bioprinter for Personalized Medicine” for financial support of this research. SK acknowledges that this work was supported by the National Science Foundation Graduate Research Fellowship (DGE-1247393). EL acknowledges the NASA CT Space Grant Consortium for the UG Research Fellowship Grant (P-1175, NNH16ZHA002C). We thank Yigitcan Eron for his contributions to development of syringe pumps.

ST and SK are founders of, and have an equity interest in QRfertile, LLC, a company that is developing microfluidic technologies for point-of-care diagnostic solutions. The authors' interests were viewed and managed in accordance with the conflict of interest policies. The authors have no other relevant affiliations or financial involvement with any organization or entity with a financial interest in or financial conflict with the subject matter or materials discussed in the manuscript apart from those disclosed.

Appendix A. Supplementary data

Supplementary data to this article can be found online at https://doi.org/10.1016/j.bprint.2019.e00044.

References

[1] S. Knowlton, S. Tasoglu, A bioprinted liver-on-a-chip for drug screening applications, Trends Biotechnol. 34 (2016) 681–682, https://doi.org/10.1016/j.tibtech.2016.05.014.
[2] S. Knowlton, B. Yenilmez, S. Tasoglu, Towards single-step biofabrication of organs on a chip via 3D printing, Trends Biotechnol. 34 (2016) 685–688, https://doi.org/10.1016/j.tibtech.2016.06.005.
[3] S. Knowlton, S. Onal, C.H. Yu, J.J. Zhao, S. Tasoglu, Bioprinting for cancer research, Trends Biotechnol. 33 (2015) 504–513, https://doi.org/10.1016/j.tibtech.2015.06.007.
[4] A. Memic, A. Navaei, B. Mirani, J.A.V. Cordova, M. Aldhahri, A. Dolatshahi-Pirouz, M. Akbari, M. Nikkhah, Bioprinting technologies for disease modeling, Biotechnol. Lett. 39 (2017) 1279–1290, https://doi.org/10.1007/s10529-017-2360-z.
[5] H.-W. Kang, S.J. Lee, I.K. Ko, C. Kengla, J.J. Yoo, A. Atala, A 3D bioprinting system to produce human-scale tissue constructs with structural integrity, Nat. Biotechnol. 34 (2016) 312–319, https://doi.org/10.1038/nbt.3413.
[6] C.-Y. Liaw, S. Ji, M. Guvendiren, Engineering 3D Hydrogels for Personalized in Vitro Human Tissue Models, 2018, https://doi.org/10.1002/adhm.201701165.
[7] A. Khademhosseini, G. Camci-Unal, 3D Bioprinting in Regenerative Engineering: Principles and Applications, CRC Pr I Llc, 2018.
[8] S. Tasoglu, U. Demirci, Bioprinting for stem cell research, Trends Biotechnol. 31 (2013) 10–19, https://doi.org/10.1016/j.tibtech.2012.10.005.
[9] S. Knowlton, C.H. Yu, F. Ersoy, S. Emadi, A. Khademhosseini, S. Tasoglu, 3D-printed microfluidic chips with patterned, cell-laden hydrogel constructs, Biofabrication 8 (2016) 25019, https://doi.org/10.1088/1758-5090/8/2/025019.
[10] S. Knowlton, S. Anand, T. Shah, S. Tasoglu , Bioprinting for neural tissue engineering, Trends Neurosci. 41 (2018) 31–46. https://doi.org/10.1016/j.tins.2017.11.001.
[11] M. Zhou, B.H. Lee, L.P. Tan, A dual crosslinking strategy to tailor rheological properties of gelatin methacryloyl, Int. J. Bioprint. 3 (No 2) (2017), https://doi.org/10.18063/IJB.2017.02.003, 2017.
[12] W. Jia, P.S. Gungor-Ozkerim, Y.S. Zhang, K. Yue, K. Zhu, W. Liu, Q. Pi, B. Byambaa, M.R. Dokmeci, S.R. Shin, A. Khademhosseini, Direct 3D bioprinting of perfusable vascular constructs using a blend bioink, Biomaterials 106 (2016) 58–68. https://doi.org/10.1016/j.biomaterials.2016.07.038.
[13] S. Knowlton, B. Yenilmez, S. Anand, S. Tasoglu, Photocrosslinking-based bioprinting: examining crosslinking schemes, Bioprinting 5 (2017) 10–18, https://doi.org/10.1016/j.bprint.2017.03.001.
[14] E. Lepowsky, M. Muradoglu, S. Tasoglu, Towards preserving post-printing cell viability and improving the resolution: past, present, and future of 3D bioprinting theory, Bioprinting 11 (2018), e00034, https://doi.org/10.1016/j.bprint.2018.e00034.
[15] S.V. M, A. Atala, 3D bioprinting of tissues and organs, Nat. Biotechnol. 32 (2014) 773–785, https://doi.org/10.1038/nbt.2958.
[16] N.A. Peppas, J.Z. Hilt, A. Khademhosseini, R. Langer, Hydrogels in biology and medicine: from molecular principles to bionanotechnology, Adv. Mater. 18 (2006) 1345–1360, https://doi.org/10.1002/adma.200501612.
[17] B.V. Slaughter, S.S. Khurshid, O.Z. Fisher, A. Khademhosseini, N.A. Peppas, Hydrogels in regenerative medicine, Adv. Mater. 21 (2009) 3307–3329, https://doi.org/10.1002/adma.200802106.
[18] J.W. Nichol, S.T. Koshy, H. Bae, C.M. Hwang, S. Yamanlar, A. Khademhosseini, Cell-laden microengineered gelatin methacrylate hydrogels, Biomaterials 31 (2010) 5536–5544, https://doi.org/10.1016/j.biomaterials.2010.03.064.
[19] L.E. Bertassoni, J.C. Cardoso, V. Manoharan, A.L. Cristino, N.S. Bhise, W.A. Araujo, P. Zorlutuna, N.E. Vrana, A.M. Ghaemmaghami, M.R. Dokmeci, A. Khademhosseini, Direct-write bioprinting of cell-laden methacrylated gelatin hydrogels, Biofabrication 6 (2014) 24105, https://doi.org/10.1088/1758-5082/6/2/024105.
[20] D.B. Kolesky, R.L. Truby, A.S. Gladman, T.A. Busbee, K.A. Homan, J.A. Lewis, 3D bioprinting of vascularized, heterogeneous cell-laden tissue constructs, Adv. Mater. 26 (2014) 3124–3130, https://doi.org/10.1002/adma.201305506.
[21] W. Zhu, B.T. Harris, L.G. Zhang, Gelatin methacrylamide hydrogel with graphene nanoplatelets for neural cell-laden 3D bioprinting, in: 2016 38th Annu. Int. Conf. IEEE Eng. Med. Biol. Soc, IEEE, 2016, pp. 4185–4188, https://doi.org/10.1109/EMBC.2016.7591649.
[22] A.D. Augst, H.J. Kong, D.J. Mooney, Alginate hydrogels as biomaterials, Macromol. Biosci. 6 (2006) 623–633, https://doi.org/10.1002/mabi.200600069.
[23] S.T. Bendtsen, S.P. Quinnell, M. Wei, Development of a novel alginate-polyvinyl alcohol-hydroxyapatite hydrogel for 3D bioprinting bone tissue engineered scaffolds, J. Biomed. Mater. Res. 105 (2017) 1457–1468, https://doi.org/10.1002/jbm.a.36036.
[24] J. Park, S.J. Lee, S. Chung, J.H. Lee, W.D. Kim, J.Y. Lee, S.A. Park, Cell-laden 3D bioprinting hydrogel matrix depending on different compositions for soft tissue engineering: characterization and evaluation, Mater. Sci. Eng. C 71 (2017) 678–684, https://doi.org/10.1016/J.MSEC.2016.10.069.
[25] K. Schütz, A.-M. Placht, B. Paul, S. Brüggemeier, M. Gelinsky, A. Lode, Three-dimensional plotting of a cell-laden alginate/methylcellulose blend: towards biofabrication of tissue engineering constructs with clinically relevant dimensions, J. Tissue Eng. Regenerat. Med. 11 (2017) 1574–1587, https://doi.org/10.1002/term.2058.
[26] B.D. Fairbanks, M.P. Schwartz, C.N. Bowman, K.S. Anseth, Photoinitiated polymerization of PEG-diacrylate with lithium phenyl-2,4,6-trimethylbenzoylphosphinate: polymerization rate and cytocompatibility, Biomaterials 30 (2009) 6702–6707, https://doi.org/10.1016/j.biomaterials.2009.08.055.
[27] Q. Gao, Y. He, J. zhong Fu, A. Liu, L. Ma, Coaxial nozzle-assisted 3D bioprinting with built-in microchannels for nutrients delivery, Biomaterials 61 (2015) 203–215, https://doi.org/10.1016/j.biomaterials.2015.05.031.
[28] C. Colosi, S.R. Shin, V. Manoharan, S. Massa, M. Costantini, A. Barbetta, M.R. Dokmeci, M. Dentini, A. Khademhosseini, Microfluidic bioprinting of heterogeneous 3D tissue constructs using low-viscosity bioink, Adv. Mater. 28 (2016) 677–684a, https://doi.org/10.1002/adma.201503310.
[29] X. Dai, L. Liu, J. Ouyang, X. Li, X. Zhang, Q. Lan, T. Xu, Coaxial 3D bioprinting of self-assembled multicellular heterogeneous tumor fibers, Sci. Rep. 7 (2017) 1–12, https://doi.org/10.1038/s41598-017-01581-y.
[30] Z. Wang, Z. Tian, W. Liu, Z. Zhong, N. Hu, Y. Zhou, L. Maggio, A.K. Miri, Coaxial extrusion bioprinting of 3D microfibrous constructs with cell-favorable gelatin methacryloyl microenvironments Coaxial extrusion bioprinting of 3D micro fi brous constructs with cell- favorable gelatin methacryloyl microenvironments, Biofabrication 10 (2018) 24102, https://doi.org/10.1088/1758-5090/aa9d44.
[31] C. a Schneider, W.S. Rasband, K.W. Eliceiri, NIH Image to ImageJ: 25 years of image analysis, Nat. Methods 9 (2012) 671–675, https://doi.org/10.1038/nmeth.2089.